Desalination and Water Treatment
www.deswater.com

doi: 10.5004/dwt.2019.24469

166 (2019) 365–376
October

In-situ synthesis of layered TiO_2 NS/UiO-66/GO with improved adsorption and photocatalytic performance toward Congo red dye

Sheng Feng*, Guiliang Zhu, Lili Cao, Runbai Wang, Shuguang Liu

School of Environmental and Safety Engineering, Changzhou University, Jiangsu 213164, China, Tel. +86-519-86330080; emails: shfeng@cczu.edu.cn (S. Feng), zhuguiliang940606@qq.com (G. Zhu), 1481977495@qq.com (L. Cao), ruibaiwang@163.com (R. Wang), shguangliu@163.com (S. Liu)

Received 23 January 2019; Accepted 28 May 2019

ABSTRACT

In the work, the layered TiO_2 NS/UiO-66/GO composites were successfully prepared through an in-situ method. Two-dimensional TiO_2 NS combined with UiO-66/GO to form a layered structure. The prepared samples were characterized by X-ray diffraction, thermogravimetric analysis, Brunauer–Emmett–Teller test, scanning electron microscopy, energy dispersive X-ray spectroscopy, X-ray photoelectron spectroscopy, UV–Vis DRS and PL spectra. TiO_2 NS/40%UiO-66/GO exhibited the most efficient adsorption (20 and 1.3 times those of TiO_2 NS and UiO-66/GO, respectively) through absorbing Congo red (CR). It also displayed the strongest photocatalytic activity (29 and 2 times those of TiO_2 NS and UiO-66/GO, respectively) for degrading CR dye under visible-light irradiation ($\lambda \geq 420$ nm). The removal rate of CR was nearly 100%. Besides, TiO_2 NS/40%UiO-66/GO showed excellent stability even after four cycling runs of adsorbing and photodegrading CR. The results showed that TiO_2 NS/UiO-66/GO composites were highly efficient adsorption and catalytic bifunctional materials. TiO_2 NS/UiO-66/GO composites provide an important basis for combining metal organic frameworks/GO with photocatalytic semiconductors to improve absorption and photocatalytic performance to better treat organic wastewaters.

Keywords: TiO_2 NS/UiO-66/GO; Layered structure; Adsorption; Photocatalysis; Congo red

1. Introduction

With the development of industry, dyes are widely used and also produce lots of dye wastewaters that seriously harm the environment and the human body. For example, Congo Red (CR) dye is hard to biodegrade and is merely metabolized to benzidine. Moreover, its exposure to organisms can cause allergic reactions. Therefore, it is important to remove dyes from wastewaters [1]. The combination of adsorption and photocatalysis could be a feasible method to effectively remove dyes. Thus, it is necessary to develop efficient adsorption and photocatalytic materials.

As a common semiconductor photocatalyst, titanium dioxide (TiO_2) is widely used because of its stable structure, strong oxidizing power and low toxicity [2–9]. Specifically, two-dimensional TiO_2 nanosheets (TiO_2 NS) with highly active (001) plane exhibit great surface reaction dynamics and strong photocatalytic activity [2,10–12]. However, pure TiO_2 NS tend to aggregate with low surface area and rapid electron–holes recombination, reducing adsorption and photocatalytic activity [2,6]. So far, some solutions have been proposed to improve photocatalytic properties such as loading precious metals [13–16] and infiltrating carbon [17–19]. It is rarely reported that the adsorption and photocatalytic performance of TiO_2-based catalysts are significantly improved. Metal organic frameworks (MOFs) are three-dimensional porous materials with high surface area and good ordered pore size, and are widely used in adsorption and catalysis [20–23]. Some special MOF types (e.g., Fe-MOF [24–28], Ti(IV)-MOF [29–31], Zr-MOF [32–35], Zn-MOF [36]) could

* Corresponding author.

have good catalytic performance under light illumination, but inefficient electrons generation and separation reduce photocatalytic activity of MOFs [37]. The combination of TiO_2 and MOFs could be a feasible method to effectively improve adsorption and photocatalytic performance [38–41]. However, general methods only promote the formation of single dispersed photosensitive TiO_2 on the surface of MOFs without forming good functional interfaces. Anatase TiO_2 follows the average surface energy order that (001) plane (0.9 J m^{-2}) > (100) plane (0.53 J m^{-2}) > (101) plane (0.44 J m^{-2}) [8,42]. In addition, the surface energy also affects the activity of (001) plane, critical to immobilize MOFs on TiO_2 NS to form more good interfaces [43]. Therefore, combining TiO_2 NS which contain numerous bare (001) planes with MOFs could promote photoelectrons transfer and enhance adsorption performance [44,45]. Besides, in order to further enhance adsorption properties, graphite oxide (GO) with a great many functional groups with oxygen is highly regarded due to its ease of coordination with the MOF metal ion and functionalization. GO can well combine with MOFs, effectively improving adsorption capacity [46,47]. Therefore, designing and constructing a layered structure by combining TiO_2 NS with MOFs/GO could be a perfect solution for improving photocatalytic and adsorption performance. UiO-66 is a MOF based on metal Zr and terephthalic acid as a ligand, exhibiting high surface area and good chemical and thermal stability, and UiO-66/GO shows stronger adsorption properties than UiO-66 [47].

Here, we developed an in-situ method to combine TiO_2 NS with UiO-66/GO to prepare layered TiO_2 NS/UiO-66/GO composites to improve adsorption and photocatalytic performance for effectively treating dye wastewaters. The adsorption and photocatalytic properties of TiO_2 NS/UiO-66/GO composites were studied by adsorbing and visible light degrading CR dye. Compared with TiO_2 NS or UiO-66/GO, TiO_2 NS/UiO-66/GO composites displayed improved absorption and photocatalytic activity. Moreover, the stability and reusability of TiO_2 NS/UiO-66/GO were investigated, and the mechanisms of adsorption and photocatalytic degradation of CR with TiO_2 NS/UiO-66/GO were discussed.

2. Experimental

2.1. Materials

The reagents applied in the research were analytical agentias and applied with no need to re-purification. Tetrabutyl titanate (98%), hydrofluoric acid (HF, 40%), zirconium chloride (IV) ($ZrCl_4$, 98%), ethanol (C_2H_5OH, 99.7%, ANHY) were purchased from China Pharmaceutical Group Chemical Reagent Co. Ltd. Terephthalic acid (H_2BDC, 99%) was purchased from Aladdin (Shanghai, China). N,N-dimethyl formamide (DMF, 99.5%, ANHY) and methanol (CH_3OH, 99.7%, ANHY) were purchased from Jiangsu strong functional chemical Limited by Share Ltd. (Changshu, Jiangsu, China). GO was purchased from Nanjing JCNANO Technology Co. Ltd. (Nanjing, Jiangsu, China).

2.1.1. Preparation of TiO_2 NS and UiO-66/GO

TiO_2 NS could be synthesized by conventional solvothermal methods [45]. First, 30 mL of tetrabutyl titanate was added to a teflon cup. Next, 3 mL of HF (40%) was slowly added dropwise into the mixture under stirring. The mixed solution was stirred for 10 min and then transferred to a stainless steel autoclave and placed in an oven at 180°C for 24 h. After the end of the reaction, the autoclave was naturally cooled to room temperature, and a white solid was collected by centrifugation and washed three times with deionized water and ethanol. After the above solid powder was dried overnight at 65°C, vacuum treatment was carried out at 120°C. Finally, it was calcined in static air at 300°C for 4 h to remove residual organic matter.

UiO-66/GO was synthesized by dispersing 10 mg GO by using ultrasound in 50 mL DMF for 8 h. $ZrCl_4$ (0.386 g) was added to a homogeneously dispersed GO solution and stirred at room temperature overnight. Then, H_2BDC (0.276 g) was poured into the above mixture and subjected to a solvothermal reaction at 120°C for 24 h. The resulting complex was centrifuged and washed several times with fresh DMF and methanol. Finally, the product was dried in a vacuum oven at 150°C [46].

2.1.2. Preparation of TiO_2 NS/UiO-66/GO composites

On the premise of pre-synthesis of TiO_2 NS, an in-situ method was used to synthesize TiO_2 NS/UiO-66/GO composites (Fig. 1) in order to achieve an enlargement of the contact surface between two components, shown to be beneficial to electrons separation in previous studies [45,48]. During the synthesis, a certain amount of TiO_2 NS (0.5 g) was first treated by sonication in 50 mL DMF for 30 min. Then, different amounts of UiO-66/GO were added. In addition, 100 mL DMF was added. The solution was treated by sonication for 30 min. It was then transferred to an oil bath and warmed to 150°C for 24 h under stirring. The resulting solid was collected by centrifugation after cooling and washed three times with fresh ethanol. Finally, the product was dried in a vacuum oven at 120°C. Here, the obtained composites are named TiO_2 NS/x%UiO-66/GO (x = 19, 31, 40, 49). In composites, m(TiO_2 NS): m(UiO-66/GO) = 1:x%.

2.2. Characterization

X-ray diffraction (XRD) was performed through adopting Cu Kα radiation (λ = 1.54056 Å) on a D/MAX2500 diffractometer worked at 40 kV and 100 mA. Thermogravimetric analysis (TGA) under nitrogen was performed with a Labsys Evo (Shanghai, China)/seteram equipment. The Brunauer–Emmett–Teller (BET) test was performed through a TriStar 3020 instrument. Microscopic images of materials were characterized through a SUPRA55 scanning electron microscope (SEM, ZEISS, Germany). The constitution of the material was explored adopting energy dispersive X-ray spectroscopy (EDS). An Escalab 250Xi analyzer was employed to measure X-ray photoelectron spectroscopy (XPS) and VBXPS to analyze the composition, valence state and valence band position of the material. A Shimadzu UV-2550 (Shanghai, China) was employed to record UV–Vis diffuse reflection spectra (DRS), which used barium sulphate ($BaSO_4$) to be the reflectance standard. An inductively coupled plasma optical emission spectrometer (ICP-OES, ICAP7400) was used to detect metallic ions in the solution after photocatalytic

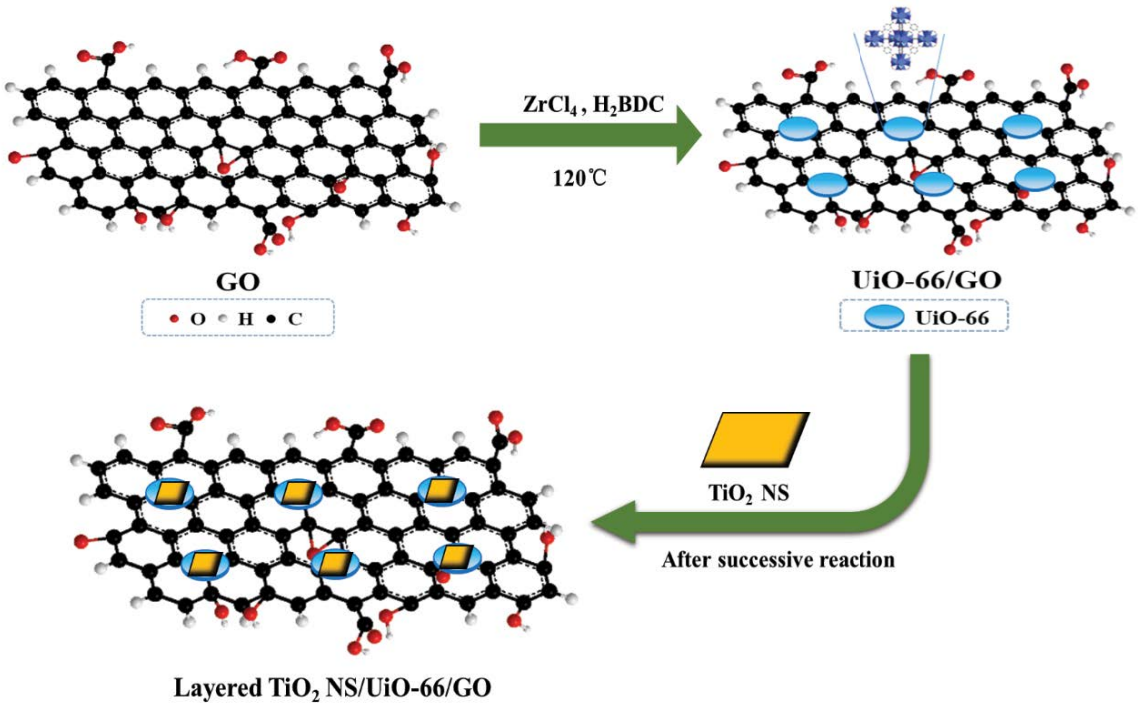

Fig. 1. Preparation methods of TiO_2 NS/UiO-66/GO composites.

reactions. Photoluminescence spectra (PL) were got on an Edinburgh FL/FS900 spectrophotometer. An electron spin resonance (ESR) spectrometer (Bruker A300, Beijing, China) was employed to detect radical species that played a decisive role in the degradation process.

2.3. Absorption and photocatalytic activity test

The absorption capacity and photocatalytic activity of TiO_2 NS/UiO-66/GO composites were measured through absorbing and photocatalytic degrading CR. 10 mg of the catalyst, 0.1 mL of 30% H_2O_2 and 50 mL of CR (50 mg L^{-1}) aqueous solution were mixed in a 50 mL colorimetric tube. At room temperature, the mixed solution was stirred without light for 1 h to reach an adsorption equilibrium and then subjected to a catalytic reaction by visible-light irradiation ($\lambda \geq 420$ nm). 3 mL CR solution was taken every 20 min and the catalyst in 3 mL CR solution was instantly separated by centrifugation. The concentration change of CR was monitored using an ultraviolet-visible spectrophotometer (UV-3600, Shimadzu, Shanghai, China) and the measurement wavelength was 496 nm.

3. Results and discussion

In TiO_2 NS/UiO-66/GO composites, TiO_2 NS/40%UiO-66/GO exhibited the most efficient adsorption and the strongest photocatalytic activity. The following discussion focused on TiO_2 NS/40%UiO-66/GO.

3.1. Physical and morphologic characterization

The construction of two components of TiO_2 NS/UiO-66/GO composites was demonstrated through performing XRD. XRD patterns of the samples are shown in Fig. 2. The samples had great crystallinity. Among them, the XRD pattern of pure TiO_2 NS described the tetragonal structure with anatase TiO_2 features [42]. The crystallographic characteristics of the prepared UiO-66/GO were the same as those reported in the published literature [46,47]. TiO_2 NS and UiO-66/GO resulted in XRD patterns with distinctive peaks such as 7.3°, 8.4°, 25.2° and 37.8° after introducing UiO-66/GO into TiO_2 NS. With the increase in the amount of UiO-66/GO during synthesis, the diffraction peak intensity of composites rose in 2θ = 7.3°, 8.4°, which illustrated the increase of the UiO-66/GO amount on TiO_2 NS.

TGA was used to test the stability of the material and to reconfirm that UiO-66/GO was added to TiO_2 NS (Fig. 3). A significant weight loss was observed initially to occur at approximately 200°C, due to the removal of solvent molecules and water molecules which were physically adsorbed by the crystals. Destruction of the structural skeleton of UiO-66/GO-TiO_2 NS was between 250°C and 550°C. TiO_2 NS exhibited extremely high thermal stability due to its slight weight loss. The composite material and UiO-66/GO were stable at about 500°C due to the insignificant changes in weight before this temperature. Above 500°C, the weight loss of the composite material and UiO-66/GO was evident, which attested that the structure was destroyed and the materials were degraded, resulting in the formation of ZrO_2 [47]. The weight loss of UiO-66/GO was about 65%, while the weight loss of TiO_2 NS/40%UiO-66/GO was about 21%, which indicated that the composite of TiO_2 NS changed the environment in which they are located, making the composite have a stronger thermal stability. The weight loss of TiO_2 NS/40%UiO-66/GO (16%) was more than that of TiO_2 NS (5%), demonstrating the presence of UiO-66/GO in the composite.

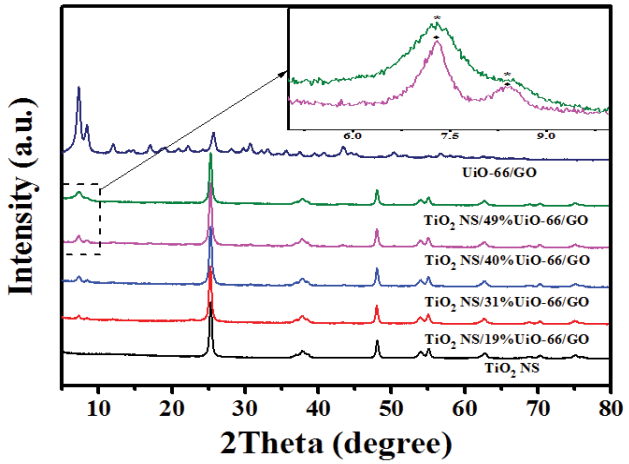

Fig. 2. XRD patterns of TiO_2 NS, UiO-66/GO and TiO_2 NS/UiO-66/GO composites (inset is the enlarged XRD patterns of TiO_2 NS/40%UiO-66/GO and TiO_2 NS/49%UiO-66/GO in the region of $2\theta = 5°–10°$).

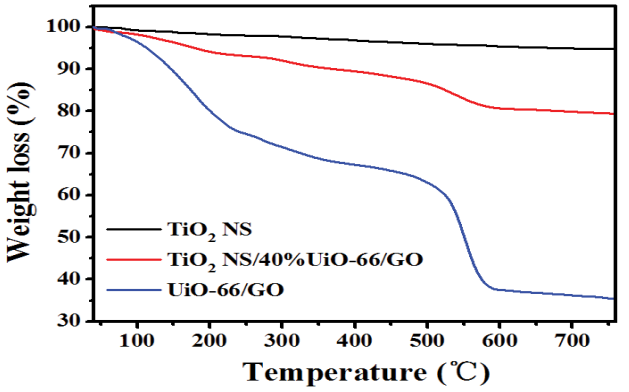

Fig. 3. TGA curves of TiO_2 NS, UiO-66/GO and TiO_2 NS/40% UiO-66/GO composites.

BET surface area and pore properties of materials were obtained through N_2 adsorption–desorption isothermal curves (Fig. 4). The isothermal curve of TiO_2 NS was a type II isotherm, which strongly confirmed the mesoporous structure [11]. The curve of UiO-66/GO was a type I isotherm which showed perpetual microporosity [47]. The curves of TiO_2 NS/UiO-66/GO composites which had the desorption lag were similar to the combination of type IV and I isothermal curves. The curves exposed that composites existed micropores and mesopores and had progressively enhanced nitrogen adsorption capacity [41,44]. Through the introduction of UiO-66/GO, the increase in surface area of TiO_2 NS/UiO-66/GO composites (Table 1) demonstrated the enhanced adsorption capacity. When the amount of UiO-66/GO added was increased (0%–49%), TiO_2 NS/UiO-66/GO composites increased gradually specific surface area from 37.0 to 305.3 $m^2\ g^{-1}$. It could be estimated that the composite porous catalyst had a larger specific surface area which could have stronger adsorption capacity and promote electron transfer to increase photocatalytic capacity.

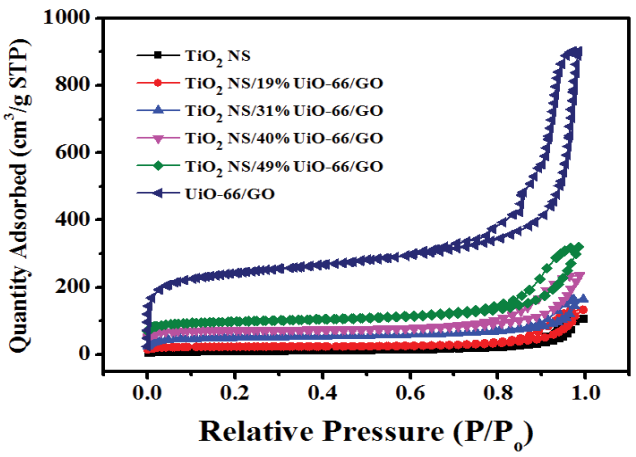

Fig. 4. N_2 adsorption–desorption isothermal curves of TiO_2 NS, UiO-66/GO and TiO_2 NS/UiO-66/GO composites.

Table 1
BET surface area of TiO_2 NS, UiO-66/GO and TiO_2 NS/UiO-66/GO composites

Sample	BET surface area ($m^2\ g^{-1}$)
TiO_2 NS	37.0
TiO_2 NS/19%UiO-66/GO	72.9
TiO_2 NS/31%UiO-66/GO	157.5
TiO_2 NS/40%UiO-66/GO	220.9
TiO_2 NS/49%UiO-66/GO	305.3
UiO-66/GO	773.6

By observing the morphological characteristics of the materials, SEM proved that TiO_2 and MOF had successfully combined (Fig. 5). In Fig. 5a, TiO_2 NS is nanoscale whose edge length was approximately 60 nm. This was obtained through observing the morphology of TiO_2 NS stacked. Moreover, obvious differences in morphology from octahedral bipyramidal anatase were observed [49]. The differences were caused by F ions which controlled morphological characteristics of samples and promoted the growth of the (001) planes [50]. In Fig. 5b, UiO-66 had an edge length of about 10–50 nm while GO had an edge length of more than 100 nm. Besides, UiO-66 was dispersed on the GO surface without aggregating. This was owing to the coordination between the metal center in UiO-66 and the oxygen group in the GO layer, which inhibited the aggregation of UiO-66 particles [51]. Fig. 5c clearly reflects the success of UiO-66/GO loading in TiO_2 NS, demonstrating the layered structure of the composites. In addition, it could be seen that the obvious interfaces were formed between TiO_2 NS, UiO-66 and GO components in TiO_2 NS/UiO-66/GO composites, and the number of layers and interfaces of TiO_2 NS/UiO-66/GO was increased as the synthesis proceeded continuously. As shown by the arrows with three different colors, the three components of TiO_2, UiO-66 and GO could be obviously seen on the composites. What deserves our attention was that TiO_2 NS were uniformly distributed in UiO-66/GO. EDS further confirmed this and the composition of the composite

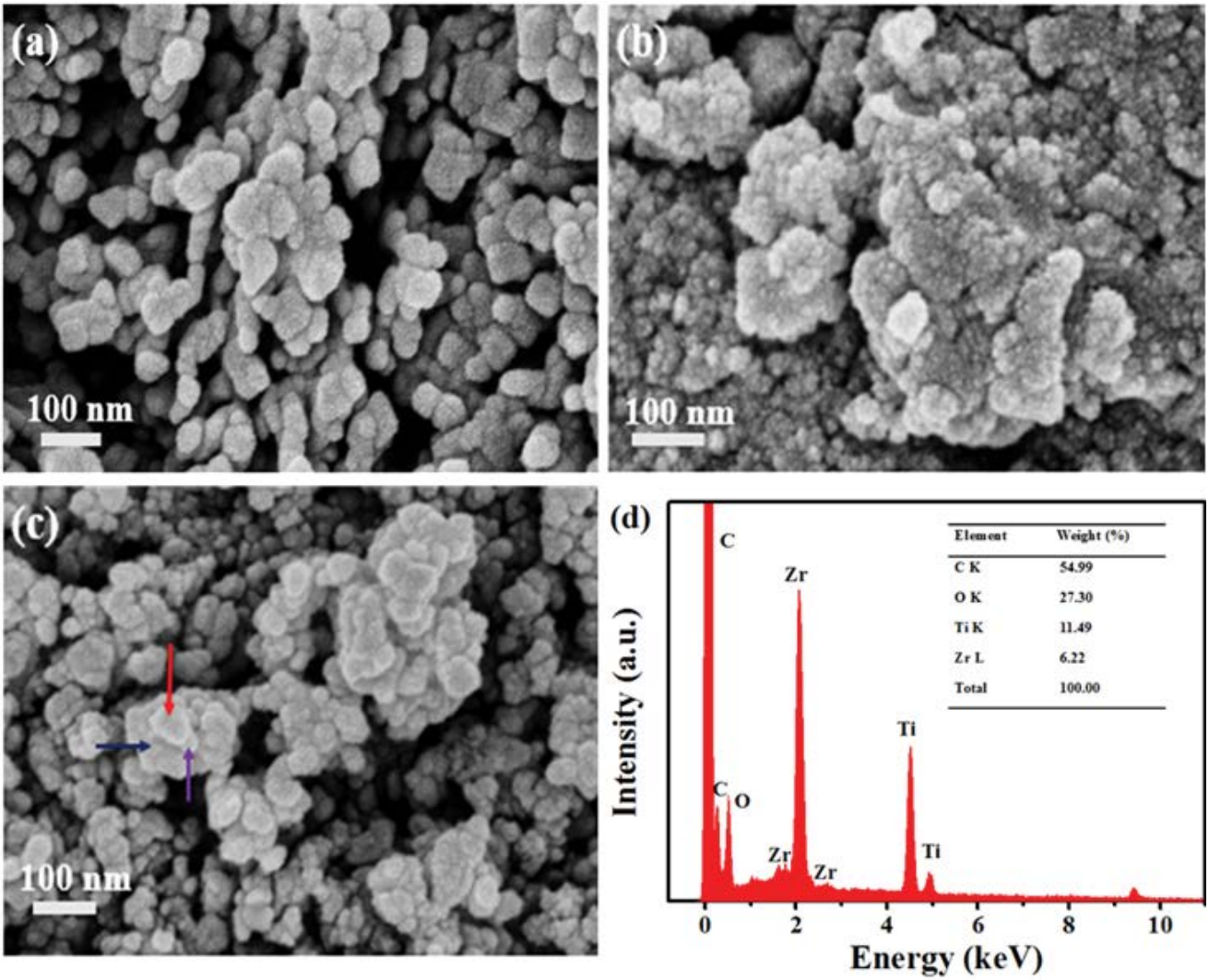

Fig. 5. SEM images of: (a) TiO_2 NS, (b) UiO-66/GO, (c) TiO_2 NS/40%UiO-66/GO with TiO_2 NS (red arrow), UiO-66 (purple arrow) and GO (navy arrow) indicated, and (d) EDS of TiO_2 NS/40%UiO-66/GO.

(Fig. 5d). The EDS spectrum displayed that the composite material contained C, O, Ti and Zr, and the four elements were uniformly distributed throughout the composite structure. In summary, SEM proved the formation of TiO_2 NS/UiO-66/GO layered structures, and showed the close interaction between the components with heterojunctions possibly formed.

XPS was used to analyze the element component and combination of pure TiO_2 NS, UiO-66/GO and TiO_2 NS/40%UiO-66/GO (Fig. 6). Fig. 6a displays that the composite existed Ti, O, F, C and Zr. It was noteworthy that F 1s 684.5 eV proved the existence of *F* element for the synthesis of TiO_2 NS [52]. The Ti 2p of the composite was split into $2p_{3/2}$ and $2p_{1/2}$, whose binding energy was approximately 458.5 and 464.3 eV (Fig. 6b), consistent with the result of Ti^{4+} in TiO_2 with a tetragonal structure [53]. Like Ti 2p, the Zr 3d of the composite was also split into $3d_{5/2}$ and $3d_{3/2}$, caused by spin-orbit coupling. Their binding energy was about 182.6 and 184.8 eV (Fig. 6c), caused by Zr^{4+} in the composite [54]. After analysis, the C 1s of the composite had four peaks. The binding energy was about 284.5, 285.4, 288.3 and 292.3 eV (Fig. 6d), respectively. Among them, C 1s 292.3 eV displayed that the composite existed C–F. 284.5, 285.4 and 288.3 eV displayed that the composite existed C=C, C–O and C=O, respectively, consistent with what UiO-66/GO contains [46,47]. In summary, the successful combination of UiO-66/GO with TiO_2 NS was further demonstrated.

Prepared materials were used to perform the photoresponse through UV–Vis DRS (Fig. 7). TiO_2 NS had a large band gap, resulting in no visible-light absorption. The "π-π" transition in the material leaded to the UV photoresponse of UiO-66/GO while UiO-66/GO also had a large band gap, resulting in no visible-light absorption [44]. Moreover, the amount of UiO-66/GO added had an important influence on the light absorption performance of TiO_2 NS/UiO-66/GO composites. It was observed that with introducing UiO-66/GO, the light absorption of composites extended from UV light to visible light, exhibiting enhanced light absorption capability. When the amount of UiO-66/GO was 40%, the degree of shift was the largest and the light absorption

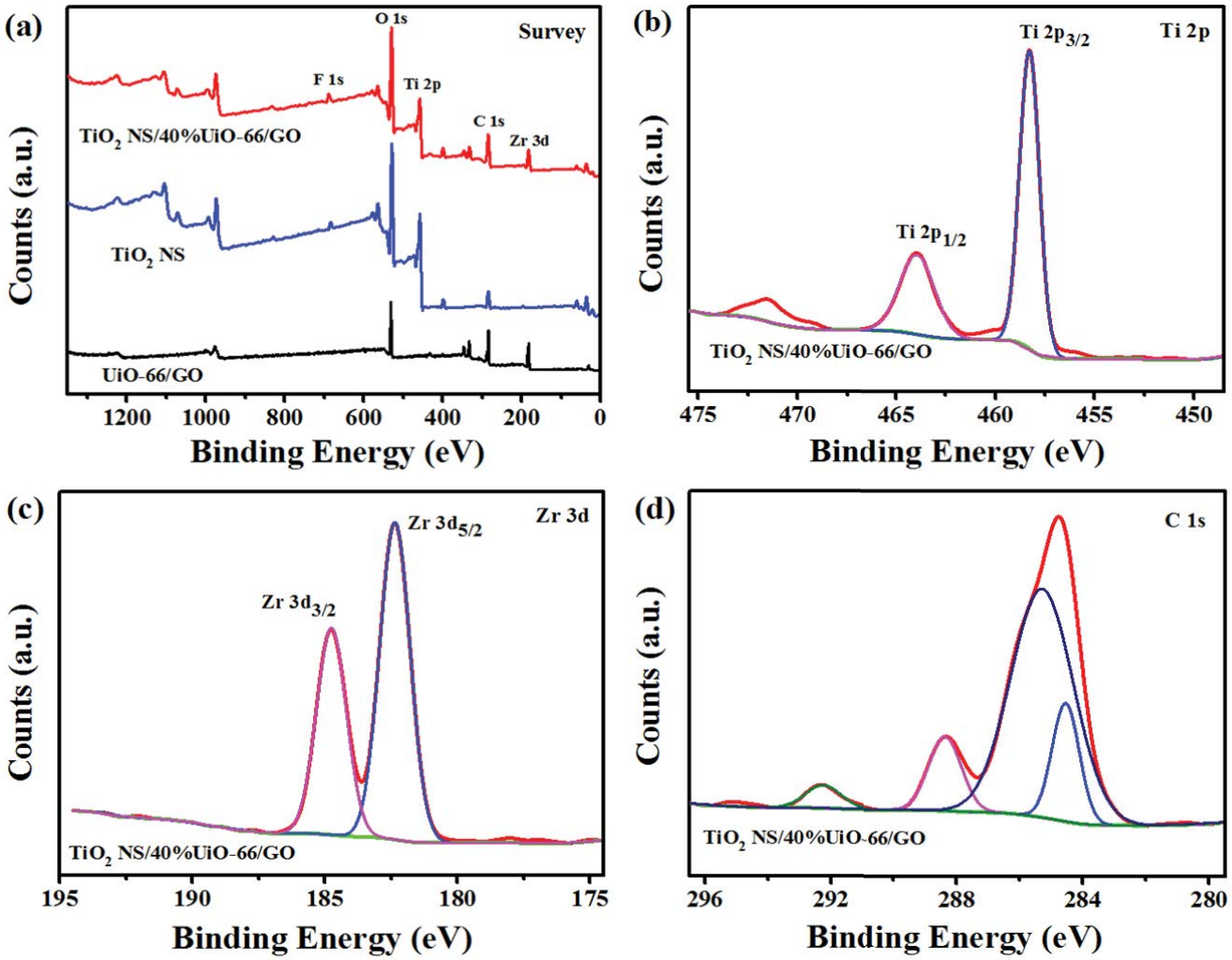

Fig. 6. XPS patterns of TiO_2 NS, UiO-66/GO and TiO_2 NS/40%UiO-66/GO: (a) survey, (b) Ti 2p, (c) Zr 3d and (d) C 1s.

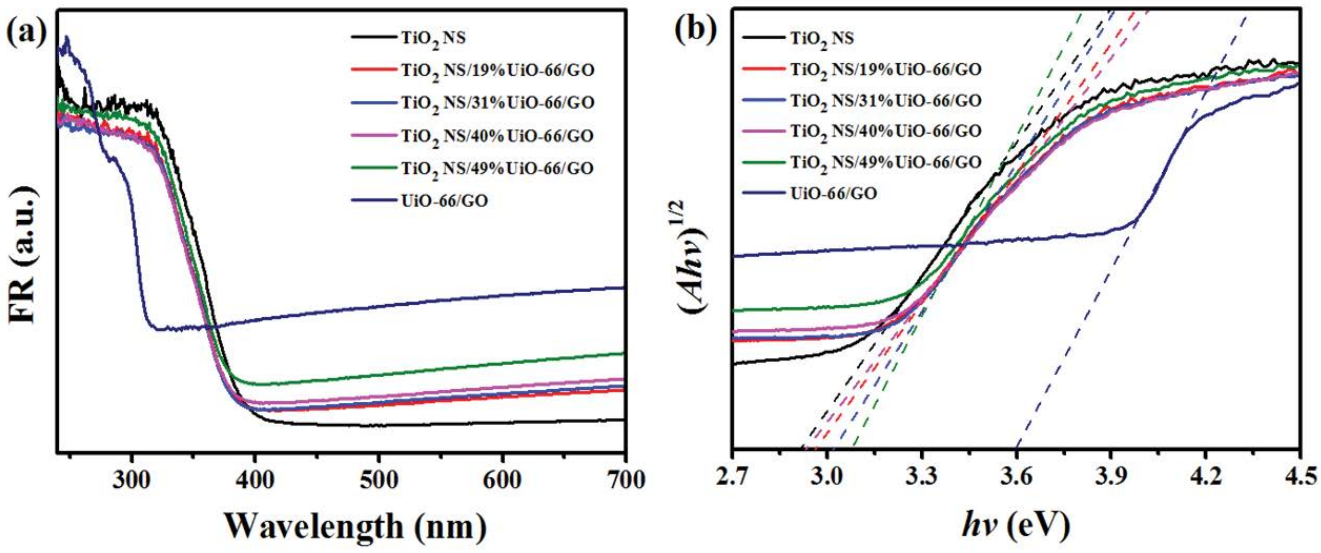

Fig. 7. (a) UV–Vis DRS spectra of TiO_2 NS, UiO-66/GO and TiO_2 NS/UiO-66/GO composites and (b) plots of $(Ahv)^{1/2}$ vs. photon energy of TiO_2 NS, UiO-66/GO and TiO_2 NS/UiO-66/GO composites.

capability was the strongest (Fig. 7a). Fig. 7b exhibits tangent intercepts of $(Ahv)^{1/2}$ vs. photon energy to obtain the band-gap energy, demonstrating that adding UiO-66/GO could promote visible-light response to TiO_2 NS/UiO-66/GO composites.

3.2. Adsorption and photocatalytic activities

Adsorbing and photodegrading CR with TiO_2 NS, UiO-66/GO and TiO_2 NS/UiO-66/GO composites (Fig. 8) were performed by absorbance detection (λ = 496 nm). It could be clearly seen that the adsorption capacity of composites was a function of the amount of UiO-66/GO added (0%–40%) (Fig. 8a). Moreover, the amount of adsorption of TiO_2 NS/40%UiO-66/GO reached the maximum, which was almost the same as that of UiO-66/GO. When the amount of UiO-66/GO was more than 40%, the amount of adsorption decreased, which was lower than that of UiO-66/GO. This might be caused by increased unused active sites in composites. In addition, CR degradation was minimal after visible light irradiation without catalyst. The most significant CR degradation occurred with TiO_2 NS/40%UiO-66/GO. This enhanced photocatalytic performance might be caused by interfaces formed by the combination of TiO_2 NS and UiO-66/GO. After adsorption and photodegradation, the removal rate of CR was nearly 100% by TiO_2 NS/40%UiO-66/GO. For better understanding, the kinetics of adsorption and photocatalysis, the data obtained from the experiment was processed through the fit of the first-order model (Eq. (1)).

$$\ln\left(\frac{C_t}{C_0}\right) = -kt \tag{1}$$

where k was kinetic rate constant. Fig. 8b displayed that kinetics of absorbing CR was a function of composites (0%–40%). With UiO-66/GO increased (0%–40%), the adsorption kinetic rate of composites increased, and reached the highest (0.059 min^{-1}) at 40%, approximately 20 and 1.3 times those of TiO_2 NS (0.003 min^{-1}) and UiO-66/GO (0.046 min^{-1}),

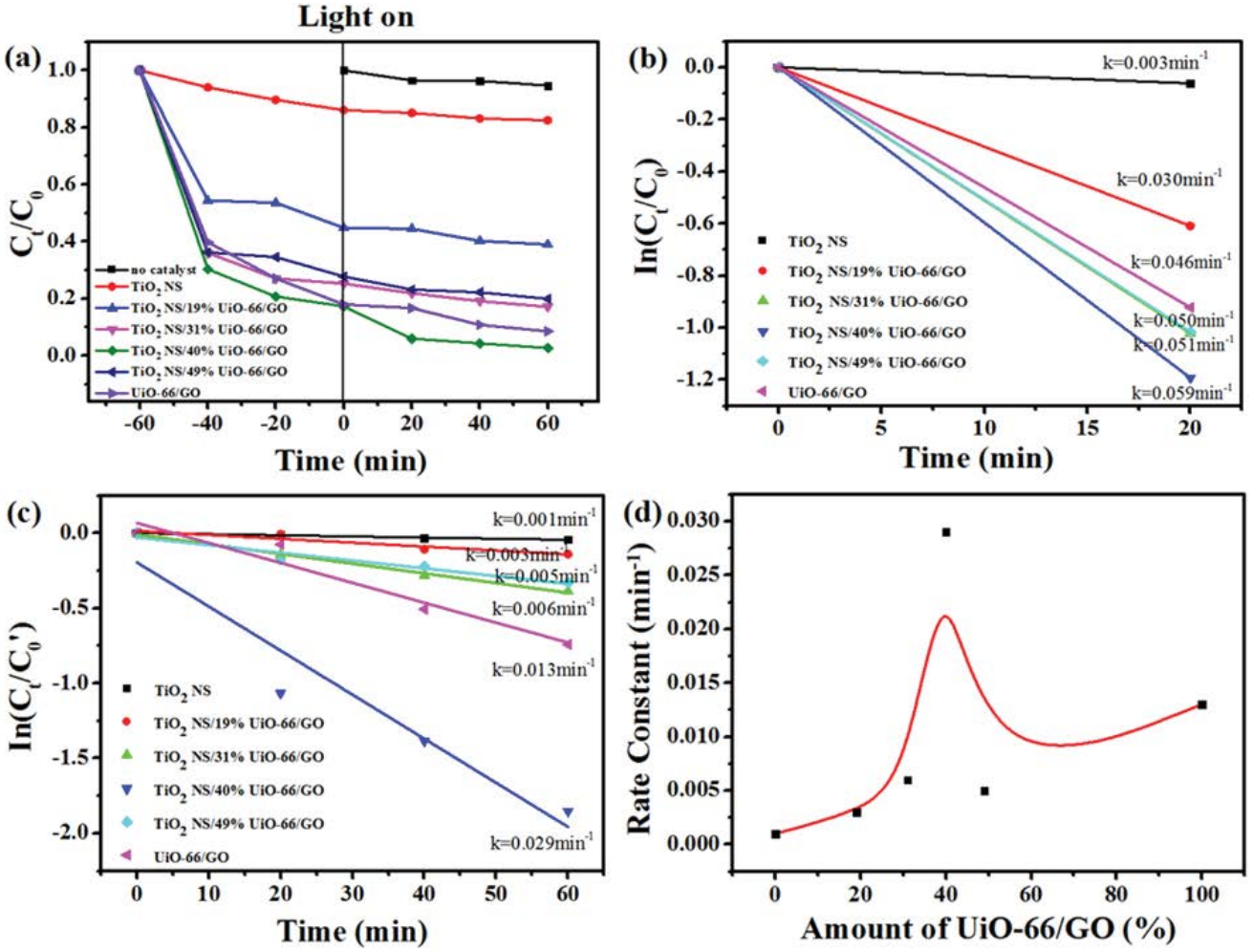

Fig. 8. (a) Absorption and photodegradation of CR with different catalysts under visible light ($\lambda \geq 420$ nm), (b) kinetics of absorbing CR with catalysts, (c) kinetics of degrading CR with catalysts and (d) catalytic rate constant ν vs. weight ratio of UiO-66/GO. C_t is the concentration of CR after reactions, C_0 is the concentration of CR before dark reaction, and C_0' is the concentration of CR before light irradiation. Reaction conditions: 10 mg of the catalyst, 50 mL 50 mg L^{-1} CR aqueous solution and 0.1 mL of 30% H_2O_2.

respectively. It was owing to high surface area and fully used active sites, providing suitable reaction conditions and beneficial to capturing organic molecules. Fig. 8c displays kinetics of photodegrading CR with catalysts. TiO_2 NS/40%UiO-66/GO exhibited the highest kinetic rate constant (0.029 min^{-1}), almost 29 and 2 times those of TiO_2 NS (0.001 min^{-1}) and UiO-66/GO (0.013 min^{-1}), respectively (Fig. 8d). It was due to rapid electrons transfer between interfaces of TiO_2 NS and UiO-66/GO, efficiently inhibiting electron–holes recombination. Notably, the adsorption and photocatalytic properties of TiO_2 NS/49%UiO-66/GO were poor, which was attributed to increased unused active sites and the aggregation of UiO-66/GO, reducing the transfer of photoelectrons between the interfaces.

To assess reusability, TiO_2 NS/40%UiO-66/GO was used to absorb and degrade CR under visible light for four circles (Fig. 9a). Before each experiment, at room temperature, the solution was stirred without light for 1 h to reach an adsorption equilibrium and then subjected to a catalytic reaction by visible-light irradiation. Absorbance and decolorization of CR in four circles confirmed that TiO_2 NS/UiO-66/GO composites had high adsorption capacity and slight deactivation. This slight reduction in photocatalytic performance might be owing to metallic ions leaching of the catalysts. To investigate metallic ions leaching of the catalysts, ICP-OES was employed to detect Ti^{4+} and Zr^{4+} in solution after photocatalytic reactions (Fig. 9b). As the number of photocatalytic reactions increased, the metallic ions leaching amount of TiO_2 NS/40%UiO-66/GO gradually increased. After four cycles, the leaching amounts of Ti^{4+} and Zr^{4+} were only 4.165 and 1.373 mg L^{-1}, respectively. The leaching amount of TiO_2 NS/40%UiO-66/GO was still low, which could not cause secondary pollution. After cycles, although the catalysts were gradually deactivated, they still maintained high stability and reusability.

PL spectra of TiO_2 NS, UiO-66/GO and TiO_2 NS/40% UiO-66/GO (excitation wavelength 250 nm) are exhibited in Fig. 10. In photocatalytic reactions, the recombination of electron–holes might reduce photocatalytic performance, releasing energy to form PL emission. Thus, low PL intensity indicated high photocatalytic property of the material. The PL intensity of UiO-66/GO was almost 0, showing a straight line. This indicated that at the excitation wavelength of 250 nm, UiO-66/GO hardly generated electrons and holes, so the recombination rate was almost 0. The PL spectrum of TiO_2 NS/40%UiO-66/GO was almost the same as that of TiO_2 NS. Comparing PL intensity, TiO_2 NS/40%UiO-66/GO was lower than TiO_2 NS. The results indicated that TiO_2 NS played the major role in the generation of electrons and holes, and electrons rapidly transferred from TiO_2 NS to UiO-66/GO, effectively promoting electron–holes separation and improving photocatalytic activity [34].

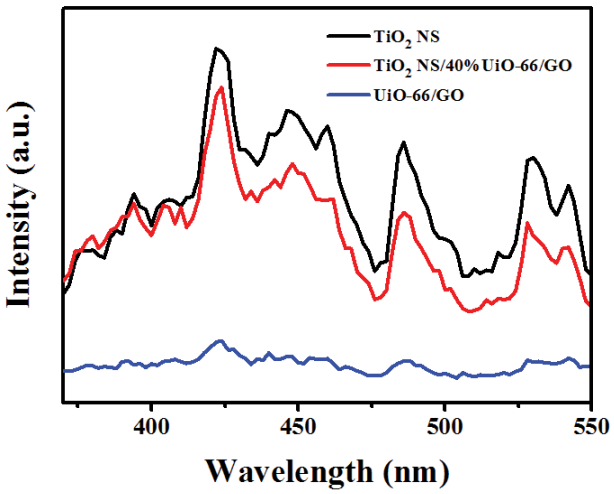

Fig. 10. PL spectra of TiO_2 NS, UiO-66/GO and TiO_2 NS/40% UiO-66/GO.

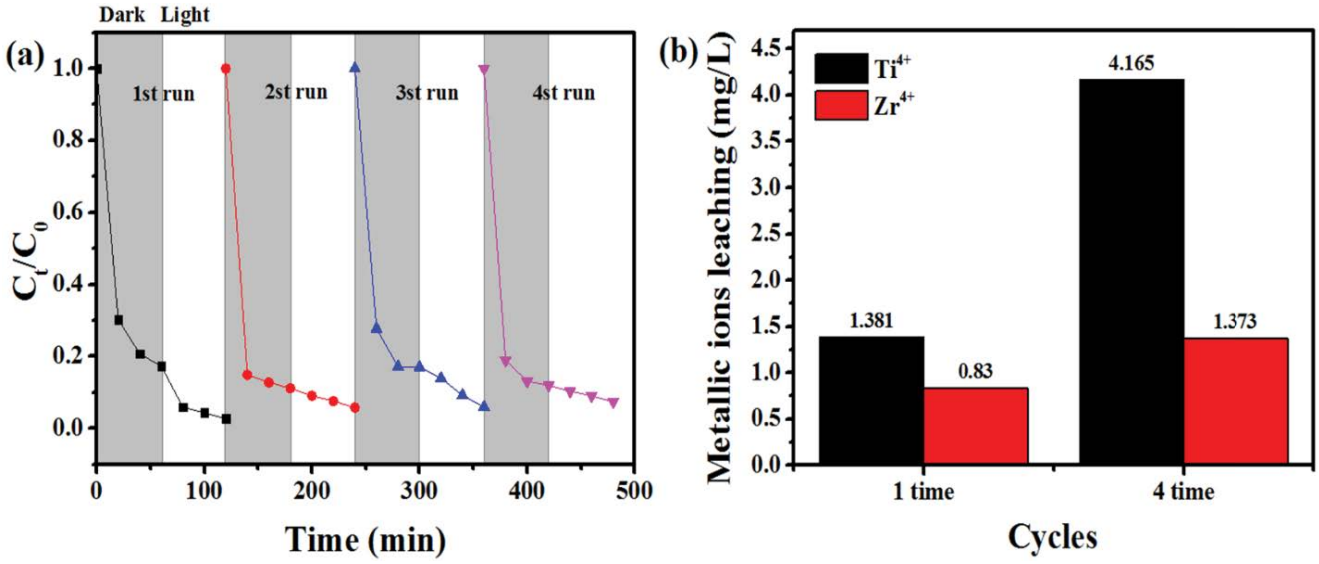

Fig. 9. (a) Adsorption and photocatalytic degradation of CR under visible light over four circles with TiO_2 NS/40%UiO-66/GO and (b) metallic ions leaching of TiO_2 NS/40%UiO-66/GO after photocatalytic reactions. Reaction conditions: 10 mg of the catalyst, 50 mL 50 mg L^{-1} CR aqueous solution and 0.1 mL of 30% H_2O_2.

3.3. Adsorption and photocatalytic mechanisms

To better interpret the high absorption capacity of composites, the mechanism for adsorbing CR with TiO_2 NS/40% UiO-66/GO was proposed (Fig. 11). The composite was mainly mesoporous and had a regular and orderly pore structure, which was favorable for capturing organic molecules, thereby enhancing the adsorption capacity. Moreover, the composite had high specific surface area with many active sites, which enhanced the adsorption capacity. The adsorption of CR with the composite was mostly owing to a great deal of π-π interactions, causing a large amount of CR molecules to be captured, which resulted in a high adsorption amount [55,56].

To better interpret the enhanced photocatalytic properties of composites, VBXPS measurements were performed to analyze the valence band of TiO_2 NS/40%UiO-66/GO (Fig. 12a). The valence band energy (E_{VB}) of TiO_2 NS/40% UiO-66/GO was obtained to be 2.81 eV. The conduction band energy (E_{CB}) of anatase TiO_2 was reported to be –0.28 eV [57]. According to Eqs. (2) and (3), E_{VB} and E_{CB} of the materials were calculated.

$$E_{VB} = \chi - E^c + 0.5E_g \quad (2)$$

$$E_{CB} = \chi - E^c - 0.5E_g \quad (3)$$

where χ was the geometric mean of the absolute electronegativity of each atom in the semiconductor, E^c was the electron free energy, which generally was 4.5 eV, and E_g was the semiconductor band-gap energy. The band-gap energy of TiO_2 NS and TiO_2 NS/40%UiO-66/GO was obtained from UV–Vis DRS spectrum (Fig. 7b). E_g (TiO_2 NS) was 2.91 eV. E_g (TiO_2 NS/40%UiO-66/GO) was 2.93 eV. Based on these, it was obtained that E_{CB} (TiO_2 NS) was 2.63 eV and E_{VB} (TiO_2 NS/40%UiO-66/GO) was –0.12 eV.

To explore radical species that played a decisive role during the degradation process, ESR measurements were performed to detect radical species. It is shown in Fig. 12b that after visible light irradiation of TiO_2 NS/40%UiO-66/GO for 60s, the peak intensity of $^{\bullet}O_2^-$ was significantly stronger than $^{\bullet}OH$. The result indicated that the concentration of $^{\bullet}O_2^-$ produced by TiO_2 NS/40%UiO-66/GO was much greater than that of $^{\bullet}OH$. Thus, $^{\bullet}O_2^-$ played a decisive role without adding H_2O_2 during degrading CR under visible light.

To explore the effect of H_2O_2 on photocatalytic degradation of CR under visible light, the degradation rate of CR by TiO_2 NS/40%UiO-66/GO with adding H_2O_2 was compared with that without H_2O_2 (Fig. 13). The photodegradation rate of CR with adding H_2O_2 (84%) was significantly higher than that without H_2O_2 (42%), proving that H_2O_2 effectively promoted photocatalytic reactions. Thus, $^{\bullet}OH$ produced by H_2O_2 [27,44,58] played an important role in the degradation process of CR after adding H_2O_2.

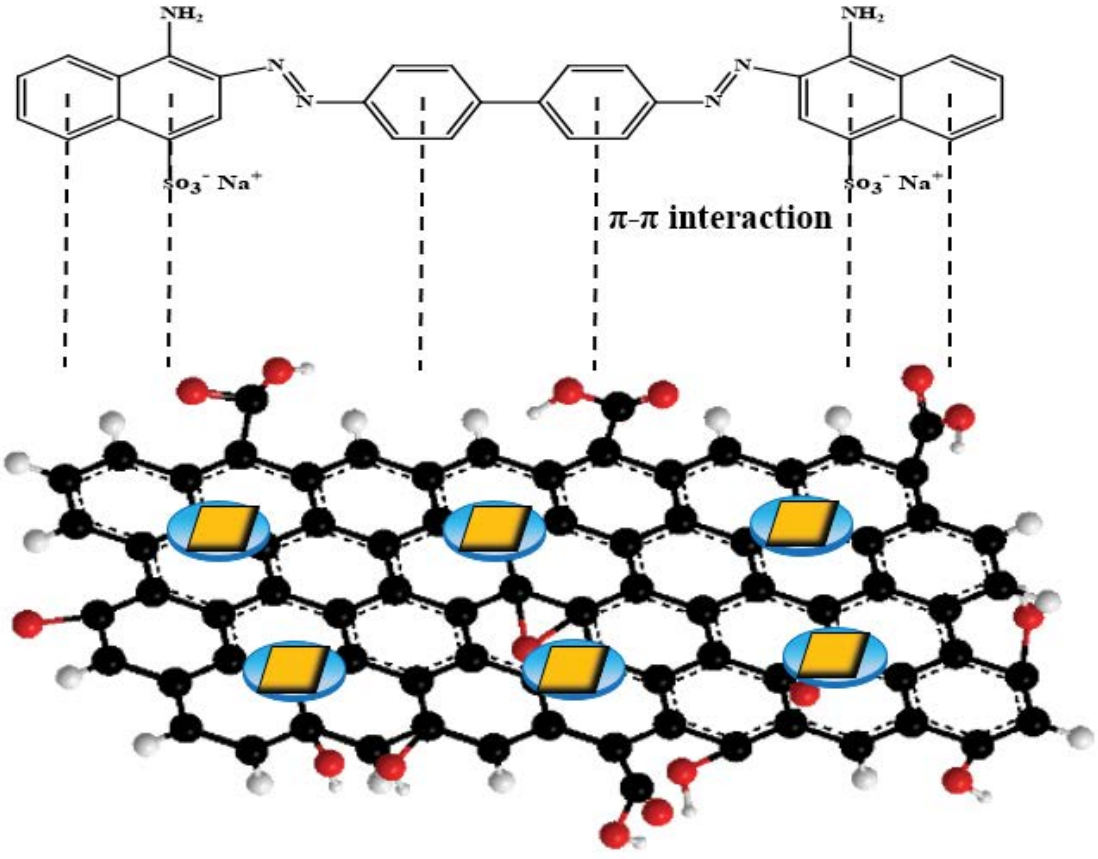

Fig. 11. Mechanism for absorbing CR with TiO_2 NS/40%UiO-66/GO.

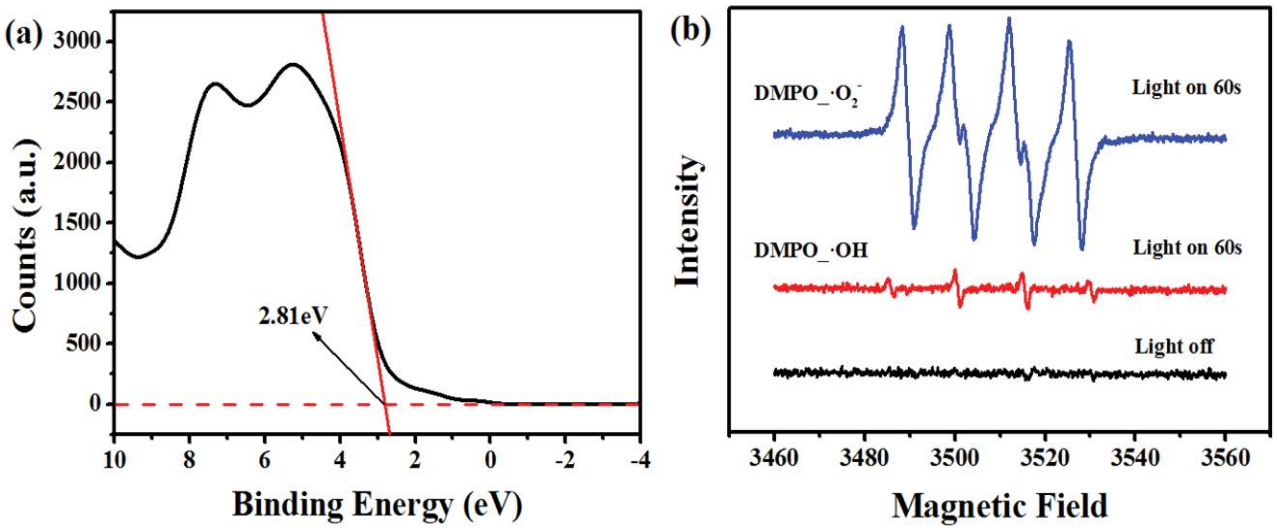

Fig. 12. (a) VBXPS of TiO_2 NS/40%UiO-66/GO and (b) ESR signals of •OH and $•O_2^-$ in TiO_2 NS/40%UiO-66/GO under visible light.

Based on above analysis and calculation, the mechanism for degrading CR with TiO_2 NS/40%UiO-66/GO under visible light was proposed (Fig. 14). In TiO_2 NS/UiO-66/GO composites, TiO_2 NS produced photoexcited electrons and holes under visible-light irradiation. The charges transferred between the inorganic semiconductor and the MOF, inhibiting electron–holes recombination [38]. Regarding TiO_2 NS/UiO-66/GO, electrons (e^-) transferred from valence band to conduction band on TiO_2 NS and holes (h^+) were generated in TiO_2 NS's valence band. Besides, the interaction between TiO_2 NS and UiO-66/GO made electrons transfer from conduction band of TiO_2 NS to that of UiO-66/GO, effectively inhibiting electron–holes recombination and improving the photocatalytic performance. Electrons (e^-) in TiO_2 NS's conduction band could react with O_2 to generate $•O_2^-$ [59] which was decisive in the degradation process of CR without adding H_2O_2. Holes (h^+) in TiO_2 NS's valence band reacted with H_2O or OH^- directly to produce •OH [59,60].

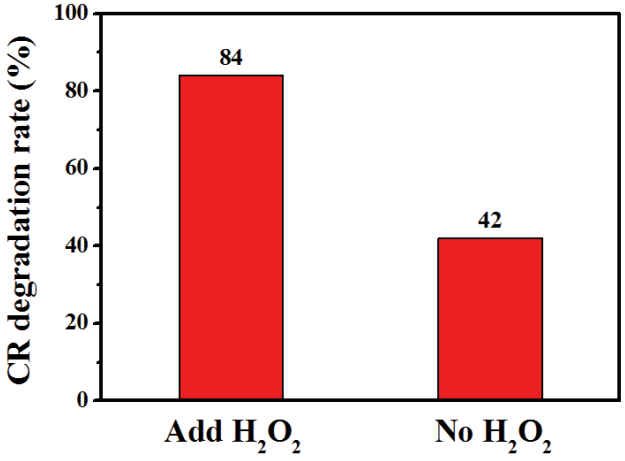

Fig. 13. Degradation rate of CR by TiO_2 NS/40%UiO-66/GO with adding H_2O_2 and without H_2O_2 under visible light.

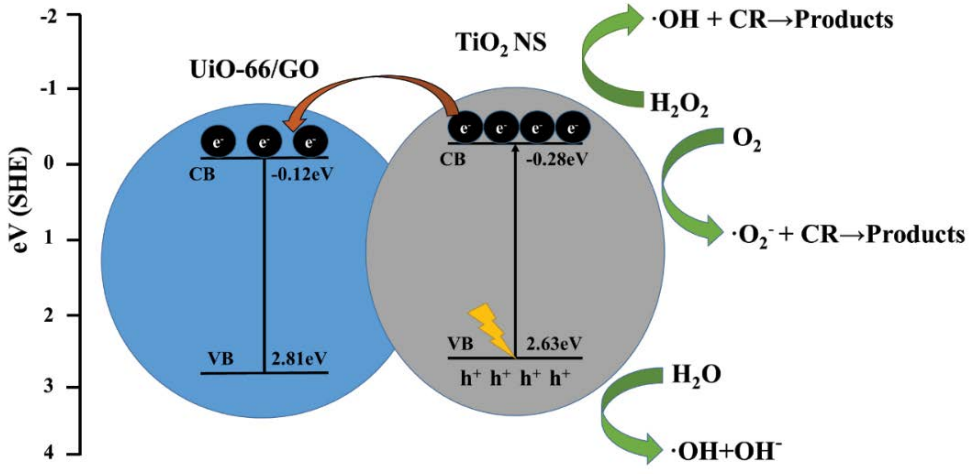

Fig. 14. Mechanism for degrading CR with TiO_2 NS/40%UiO-66/GO under visible light.

In addition, the addition of H_2O_2 could promote photocatalytic reactions. H_2O_2 accepted electrons and reacted with TiO_2 NS under visible-light irradiation to generate lots of $^{\bullet}OH$ [27,44,58]. Intrinsically, both $^{\bullet}O_2^-$ and $^{\bullet}OH$ played an important role in directly oxidizing the absorbed organic molecules [44,60].

4. Conclusion

In the study, layered TiO_2 NS/UiO-66/GO composites were well prepared by an in-situ method for effectively treating dye wastewaters. Two-dimensional TiO_2 NS combined with UiO-66/GO to form a layered structure, improving absorption and photocatalytic performance. The composites especially TiO_2 NS/40%UiO-66/GO showed the most efficient adsorption (20 and 1.3 times those of TiO_2 NS and UiO-66/GO, respectively) through absorbing CR. It also exhibited the strongest photocatalytic activity (29 and 2 times those of TiO_2 NS and UiO-66/GO, respectively) for degrading CR dye under visible light ($\lambda \geq 420$ nm). The removal rate of CR was nearly 100%. The improved adsorption was owing to π–π interactions, high surface area of the composite and fully used active sites. The enhanced photocatalytic property was attributed to the rapid transfer of photoexcited electrons from conduction band of TiO_2 NS to that of UiO-66/GO, inhibiting electron–holes recombination. The study would provide an important basis for combining MOFs/GO with photocatalytic semiconductors to improve absorption and photocatalytic performance to better treat organic wastewaters.

Acknowledgments

The authors would like to sincerely acknowledge the financial supports from the National Natural Science Foundation of China (No. 41371446 and No. 41271498), the National Social Science Foundation of China (No. 16BJL074) and SKLECRA2014OFP10.

References

[1] Y. Bao, M. Qin, Y. Yu, L. Zhang, H. Wu, Facile fabrication of porous $NiCo_2O_4$ nanosheets with high adsorption performance toward Congo red, J. Phys. Chem. Solids, 124 (2019) 289–295.
[2] H. Li, H. Liu, Q. Zhang, C. Wang, T. Li, Synthesis and photocatalytic activity of ring-like anatase TiO_2 with {001} facts exposed, Ceram. Int., 41 (2015) 8717–8722.
[3] S. Liu, Z. Wang, C. Yu, H.B. Wu, G. Wang, Q. Dong, J. Qiu, A. Eychmüller, X.W. David Lou, A flexible TiO_2(B)-based battery electrode with superior power rate and ultralong cycle life, Adv. Mater., 25 (2013) 3462–3467.
[4] C. Wang, F. Wang, Y. Zhao, Y. Li, Q. Yue, Y. Liu, Y. Liu, A.A. Elzatahry, A. Al-Enizi, Y. Wu, Y. Deng, D. Zhao, Hollow TiO_{2-X} porous microspheres composed of well-crystalline nanocrystals for high-performance lithium-ion batteries, Nano Res., 9 (2016) 165–173.
[5] C.B.D. Marien, T. Cottineau, D. Robert, P. Drogui, TiO_2 nanotube arrays: influence of tube length on the photocatalytic degradation of Paraquat, Appl. Catal., B, 194 (2016) 1–6.
[6] F. Cao, J. Xiong, F. Wu, Q. Liu, Z. Shi, Y. Yu, X. Wang, L. Li, Enhanced photoelectrochemical performance from rationally designed anatase/rutile TiO_2 heterostructures, ACS Appl. Mater. Interfaces, 8 (2016) 12239.
[7] V. Vaiano, G. Iervolino, D. Sannino, J.J. Murcia, M.C. Hidalgo, P. Ciambelli, J.A. Navío, Photocatalytic removal of patent blue V dye on Au-TiO_2 and Pt-TiO_2 catalysts, Appl. Catal., B, 188 (2016) 134–146.
[8] K. Chen, Z. Jiang, J. Qin, Y. Jiang, R. Li, H. Tang, X. Yang, Synthesis and improved photocatalytic activity of ultrathin TiO_2 nanosheets with nearly 100% exposed (001) facets, Ceram. Int., 40 (2014) 16817–16823.
[9] Z. Lu, F. Chen, M. He, M. Song, Z. Ma, W. Shi, Y. Yan, J. Lan, F. Li, P. Xiao, Microwave synthesis of a novel magnetic imprinted TiO_2 photocatalyst with excellent transparency for selective photodegradation of enrofloxacin hydrochloride residues solution, Chem. Eng. J., 249 (2014) 15–26.
[10] C. Hu, X. Zhang, W. Li, Y. Yan, G. Xi, H. Yang, J. Li, H. Bai, Large-scale, ultrathin and (001) facet exposed TiO_2 nanosheet superstructures and their applications in photocatalysis, J. Mater. Chem. A, 2 (2014) 2040–2043.
[11] G. Xiang, T. Li, J. Zhuang, X. Wang, Large-scale synthesis of metastable TiO_2(B) nanosheets with atomic thickness and their photocatalytic properties, Chem. Commun., 46 (2010) 6801.
[12] P. Wang, Y. Li, Z. Liu, J. Chen, Y. Wu, M. Guo, P. Na, In-situ deposition of Ag_3PO_4 on TiO_2 nanosheets dominated by (001) facets for enhanced photocatalytic activities and recyclability, Ceram. Int., 43 (2017) 11588–11595.
[13] D. Li, J. Jia, T. Zheng, X. Cheng, X. Yu, Construction and characterization of visible light active Pd nano-crystallite decorated and C-N-S-co-doped TiO_2 nanosheet array photoelectrode for enhanced photocatalytic degradation of acetylsalicylic acid, Appl. Catal., B, 188 (2016) 259–271.
[14] J. Yu, L. Qi, M. Jaroniec, Hydrogen production by photocatalytic water splitting over Pt/TiO_2 nanosheets with exposed (001) facets, J. Phys. Chem. C, 114 (2010) 13118–13125.
[15] S. Wang, J.-H. Yun, B. Luo, T. Butburee, P. Peerakiatkhajohn, S. Thaweesak, M. Xiao, L. Wang, Recent progress on visible light responsive heterojunctions for photocatalytic applications, J. Mater. Sci. Technol., 33 (2017) 1–22.
[16] Y. Zhang, T. Wang, M. Zhou, Y. Wang, Z. Zhang, Hydrothermal preparation of Ag-TiO_2 nanostructures with exposed {001}/{101} facets for enhancing visible light photocatalytic activity, Ceram. Int., 43 (2016) 3118–3126.
[17] W.-S. Wang, D.-H. Wang, W.-G. Qu, L.-Q. Lu, A.-W. Xu, Large ultrathin anatase TiO_2 nanosheets with exposed {001} facets on graphene for enhanced visible light photocatalytic activity, J. Phys. Chem. C, 116 (2012) 19893–19901.
[18] W. Guo, F. Zhang, C. Lin, Z.L. Wang, Direct growth of TiO_2 nanosheet arrays on carbon fibers for highly efficient photocatalytic degradation of methyl orange, Adv. Mater., 24 (2012) 4761–4764.
[19] J. Li, S. Wang, Y. Du, W. Liao, Enhanced photocatalytic performance of TiO_2@C nanosheets derived from two-dimensional Ti_2CT_x, Ceram. Int., 44 (2018) 7042–7046.
[20] B.A. Al-Maythalony, O. Shekhah, R. Swaidan, Y. Belmabkhout, I. Pinnau, M. Eddaoudi, Quest for anionic MOF membranes: continuous sod-ZMOF membrane with CO_2 adsorption-driven selectivity, J. Am. Chem. Soc., 137 (2015) 1754–1757.
[21] Y.-P. Yuan, L.-S. Yin, S.-W. Cao, G.-S. Xu, C.-H. Li, C. Xue, Improving photocatalytic hydrogen production of metal–organic framework UiO-66 octahedrons by dye-sensitization, Appl. Catal., B, 168–169 (2015) 572–576.
[22] I. Hod, M.D. Sampson, P. Deria, C.P. Kubiak, O.K. Farha, J.T. Hupp, Fe-porphyrin-based metal–organic framework films as high-surface concentration, heterogeneous catalysts for electrochemical reduction of CO_2, ACS Catal., 5 (2015) 6302–6309.
[23] I. Spanopoulos, C. Tsangarakis, E. Klontzas, E. Tylianakis, G. Froudakis, K. Adil, Y. Belmabkhout, M. Eddaoudi, P.N. Trikalitis, Reticular synthesis of HKUST-like tbo-MOFs with enhanced CH_4 storage, J. Am. Chem. Soc., 138 (2016) 1568–1574.
[24] K.G.M. Laurier, F. Vermoortele, R. Ameloot, D.E. De Vos, J. Hofkens, M.B.J. Roeffaers, Iron(III)-based metal–organic frameworks as visible light photocatalysts, J. Am. Chem. Soc., 135 (2013) 14488–14491.
[25] W.T. Xu, L. Ma, F. Ke, F.-M. Peng, G.-S. Xu, Y.-H. Shen, J.-F. Zhu, L.-G. Qiu, Y.-P. Yuan, Metal–organic frameworks MIL-88A hexagonal microrods as a new photocatalyst for efficient

decolorization of methylene blue dye, Dalton Trans., 43 (2014) 3792–3798.
[26] D. Wang, R. Huang, W. Liu, D. Sun, Z. Li, Fe-based MOFs for photocatalytic CO_2 reduction: role of coordination unsaturated sites and dual excitation pathways, ACS Catal., 4 (12) (2014).
[27] D. Wang, M. Wang, Z. Li, Fe-based metal–organic frameworks for highly selective photocatalytic benzene hydroxylation to phenol, ACS Catal., 5 (2015) 6852–6857.
[28] H.-Q. Xu, J. Hu, D. Wang, Z. Li, Q. Zhang, Y. Luo, S.-H. Yu, H.-L. Jiang, Visible-light photoreduction of CO_2 in a metal–organic framework: boosting electron–hole separation via electron trap states, J. Am. Chem. Soc., 137 (2015) 13440–13443.
[29] S. Vaesen, V. Guillerm, Q. Yang, A.D. Wiersum, B. Marszalek, B. Gil, A. Vimont, M. Daturi, T. Devic, P.L. Llewellyn, G. Maurin, G. De Weireld, A robust amino-functionalized titanium(IV) based MOF for improved separation of acid gases, Chem. Commun., 49 (2013) 10082–10084.
[30] Y. Fu, D. Sun, Y. Chen, R. Huang, Z. Ding, X. Fu, Z. Li, An amine-functionalized titanium metal–organic framework photocatalyst with visible-light-induced activity for CO_2 reduction, Angew. Chem. Int. Ed., 51 (2012) 3364–3367.
[31] D. Sun, Y. Lin, Z. Li, Visible-light-assisted aerobic photocatalytic oxidation of amines to imines over NH_2-MIL-125(Ti), Appl. Catal., B, 164 (2015) 428–432.
[32] S.C. Gomes, I. Luz, F.X. Llabrés i Xamena, A. Corma, H. García, Water stable Zr–benzenedicarboxylate metal–organic frameworks as photocatalysts for hydrogen generation, Chem. Eur. J., 16 (2010) 11133–11138.
[33] D. Sun, Y. Fu, W. Liu, L. Ye, D. Wang, L. Yang, X. Fu, Z. Li, Studies on photocatalytic CO_2 reduction over NH_2-Uio-66(Zr) and its derivatives: towards a better understanding of photocatalysis on metal–organic frameworks, Chem. Eur. J., 19 (2013) 14279–14285.
[34] J.-D. Xiao, Q. Shang, Y. Xiong, Q. Zhang, Y. Luo, S.-H. Yu, H.-L. Jiang, Boosting photocatalytic hydrogen production of a metal–organic framework decorated with platinum nanoparticles: the platinum location matters, Angew. Chem. Int. Ed., 55 (2016) 9389–9393.
[35] D. Sun, W. Liu, M. Qiu, Y. Zhang, Z. Li, Introduction of a mediator for enhancing photocatalytic performance *via* post-synthetic metal exchange in metal–organic frameworks (MOFs), Chem. Commun., 51 (2015) 10765–10765.
[36] X. Zeng, L. Huang, C. Wang, J. Wang, J. Li, X. Luo, Sono-crystallization of ZIF-8 on electrostatic spinning TiO_2 nanofibers surface with enhanced photocatalysis property through synergistic effect, ACS Appl. Mater. Interfaces, 8 (2016) 20274.
[37] F. Ke, L. Wang, J. Zhu, Facile fabrication of CdS-metal-organic framework nanocomposites with enhanced visible-light photocatalytic activity for organic transformation, Nano Res., 8 (2015) 1834–1846.
[38] J. He, Z. Yan, J. Wang, J. Xie, L. Jiang, Y. Shi, F. Yuan, F. Yu, Y. Sun, Significantly enhanced photocatalytic hydrogen evolution under visible light over CdS embedded on metal–organic frameworks, Chem. Commun., 49 (2013) 6761–6763.
[39] H. Sheng, D. Chen, N. Li, Q. Xu, H. Li, J. He, J. Lu, Urchin-inspired TiO_2@MIL-101 double-shell hollow particles: adsorption and highly efficient photocatalytic degradation of hydrogen sulfide, Chem. Mater., 29 (2017) 5612–5616.
[40] S. Abedi, A. Morsali, Ordered mesoporous metal–organic frameworks incorporated with amorphous TiO_2 as photocatalyst for selective aerobic oxidation in sunlight irradiation, ACS Catal., 14 (1995) 1398–1403.
[41] R. Li, J. Hu, M. Deng, H. Wang, X. Wang, Y. Hu, H.-L. Jiang, J. Jiang, Q. Zhang, Y. Xie, Y. Xiong, Integration of an inorganic semiconductor with a metal–organic framework: a platform for enhanced gaseous photocatalytic reactions, Adv. Mater., 26 (2014) 4783.
[42] G. Liu, H.G. Yang, J. Pan, Y.Q. Yang, G.Q. Lu, H.M. Cheng, Titanium dioxide crystals with tailored facets, Chem. Rev., 114 (2014) 9559–9612.
[43] B. Liu, Y. Huang, Y. Wen, L. Du, W. Zeng, Y. Shi, F. Zhang, G. Zhu, X. Xu, Y. Wang, Highly dispersive {001} facets-exposed nanocrystalline TiO_2 on high quality graphene as a high performance photocatalyst, J. Mater. Chem., 22 (2012) 7484–7491.
[44] X. Liu, R. Dang, W. Dong, X. Huang, J. Tang, H. Gao, G. Wang, A sandwich-like heterostructure of TiO_2 nanosheets with MIL-100(Fe): a platform for efficient visible-light-driven photocatalysis, Appl. Catal., B, 209 (2017) 506–513.
[45] A. Crake, K.C. Christoforidis, A. Kafizas, S. Zafeiratos, C. Petit, CO_2 capture and photocatalytic reduction using bifunctional TiO_2/MOF nanocomposites under UV–vis irradiation, Appl. Catal., B, 210 (2017) 131–140.
[46] J. Ma, X. Guo, Y. Ying, D. Liu, C. Zhong, Composite ultrafiltration membrane tailored by MOF@GO with highly improved water purification performance, Chem. Eng. J., 313 (2016) 890–898.
[47] Y. Cao, Y. Zhao, Z. Lv, F. Song, Q. Zhong, Preparation and enhanced CO_2 adsorption capacity of UiO-66/graphene oxide composites, J. Ind. Eng. Chem., 27 (2015) 102–107.
[48] J. Hong, C. Chen, F.E. Bedoya, G.H. Kelsall, D. O'Hare, C. Petit, Carbon nitride nanosheet/metal–organic framework nanocomposites with synergistic photocatalytic activities, Catal. Sci. Technol., 6 (2016) 5042–5051.
[49] K.C. Christoforidis, A. Iglesias-Juez, S.J.A. Figueroa, M. Di Michiel, M.A. Newton, M. Fernández-García, Structure and activity of iron-doped TiO_2-anatase nanomaterials for gas-phase toluene photo-oxidation, Catal. Sci. Technol., 3 (2012) 626–634.
[50] Y. Cao, Q. Li, C. Li, J. Li, J. Yang, Surface heterojunction between (001) and (101) facets of ultrafine anatase TiO_2 nanocrystals for highly efficient photoreduction CO_2 to CH_4, Appl. Catal., B, 198 (2016) 378–388.
[51] X. Sun, Q. Xia, Z. Zhao, Y. Li, Z. Li, Synthesis and adsorption performance of MIL-101(Cr)/graphite oxide composites with high capacities of *n*-hexane, Chem. Eng. J., 239 (2014) 226–232.
[52] H.G. Yang, C.H. Sun, S.Z. Qiao, J. Zou, G. Liu, S.C. Smith, H.M. Cheng, G.Q. Lu, Anatase TiO_2 single crystals with a large percentage of reactive facets, Nature, 453 (2008) 638.
[53] Z. Sun, T. Liao, Y. Dou, S.M. Hwang, M.-S. Park, L. Jiang, J.H. Kim, S.X. Dou, Generalized self-assembly of scalable two-dimensional transition metal oxide nanosheets, Nat. Commun., 5 (2014) 3813.
[54] Q. Liang, S. Cui, C. Liu, S. Xu, C. Yao, Z. Li, Construction of CdS@UIO-66-NH_2 core-shell nanorods for enhanced photocatalytic activity with excellent photostability, J. Colloid Interface Sci., 524 (2018) 379–387.
[55] Y. Pi, X. Li, Q. Xia, J. Wu, Y. Li, J. Xiao, Z. Li, Adsorptive and photocatalytic removal of persistent organic pollutants (POPs) in water by metal-organic frameworks (MOFs), Chem. Eng. J., 337 (2017) 351–371.
[56] Z. Hasan, S.H. Jhung, Removal of hazardous organics from water using metal-organic frameworks (MOFs): plausible mechanisms for selective adsorptions, J. Hazard. Mater., 283 (2015) 329–339.
[57] D.O. Scanlon, C.W. Dunnill, J. Buckeridge, S.A. Shevlin, A.J. Logsdail, S.M. Woodley, C.R.A. Catlow, M.J. Powell, R.G. Palgrave, I.P. Parkin, G.W. Watson, T.W. Keal, P. Sherwood, A. Walsh, A.A. Sokol, Band alignment of rutile and anatase TiO_2, Nat. Mater., 12 (2013) 798–801.
[58] L. Ai, C. Zhang, L. Li, J. Jiang, Iron terephthalate metal–organic framework: revealing the effective activation of hydrogen peroxide for the degradation of organic dye under visible light irradiation, Appl. Catal., B, 148–149 (2014) 191–200.
[59] Z. Lu, Z. Yu, J. Dong, M. Song, Y. Liu, X. Liu, Z. Ma, H. Su, Y. Yan, P. Huo, Facile microwave synthesis of a Z-scheme imprinted $ZnFe_2O_4$/Ag/PEDOT with the specific recognition ability towards improving photocatalytic activity and selectivity for tetracycline, Chem. Eng. J., 337 (2018) 228–241.
[60] Z. Lu, J. Peng, M. Song, Y. Liu, X. Liu, P. Huo, H. Dong, S. Yuan, Z. Ma, S. Han, Improved recyclability and selectivity of environment-friendly MFA-based heterojunction imprinted photocatalyst for secondary pollution free tetracycline orientation degradation, Chem. Eng. J., 360 (2019) 1262–1276.